Charge Collection Distance of Diamond Vertex Detectors

by

Brian P. Josey

Mentors: Sally Seidel and Martin Hoeferkamp

Undergraduate Honors Thesis
University of New Mexico
Department of Physics and Astronomy
Albuquerque, New Mexico

May 31, 2012

Abstract

As currently used in the ATLAS detector at the Large Hadron Collider (LHC) in Geneva, Switzerland, vertex detectors are composed primarily of silicon sensors that image particle tracks by detecting the creation of electron-hole pairs caused by the excitation of the silicon atoms. I investigated, in the framework of the RD-42 collaboration, the potential of replacing these silicon detectors with detectors made out of diamond. Diamond is advantageous due to its high radiation hardness, or resistance to to changes in its performance when exposed to a radiation environment, such as that found at the LHC. In order to determine the potential value of using diamonds as a detector medium I measured the charge collection of diamond samples before and after irradiation. For a non-irradiated diamond sample, I measured a charge collection of $1920 \pm 18 e^-$. This sample was then irradiated with a total fluence of 2.74×10^{15} 800 MeV p/cm^2 and had a charge collection of $1160 \pm 19 e^-$, 60.4 % of the initial value. These measurements indicate the potential utility of diamond as a detector medium and can then be used to guide the necessary upgrades required for the High Luminosity LHC.

Acknowledgments

Contents

List of Tables

List of Figures

Chapter 1

Introduction

For this thesis, I researched the possibility of using artificial polycrystalline diamonds as an upgrade for the vertex detectors in ATLAS, one of the four detectors at the Large Hadron Collider (LHC) in Geneva, Switzerland. Currently, there is an interest in upgrading the luminosity, or number of protons per square centimeter per second being accelerated by the LHC in the near future. This process will create a higher yield in data, and provide more statistics for data analysis. While this upgrade to a High-Luminosity LHC will provide more information for particle physics, there are technical issues that such an upgrade will face [1]. Of the many technical issues, one in particular is the increase in fluence, or total number or particles, incident on the detectors. In collaboration with the RD-42 collaboration, I investigated the amount of charge collected by diamond vertex detectors before and after being irradiated to see how damage from the radiation affects their charge collection.

In this chapter, I will provide a brief overview of the LHC, ATLAS and the High-Luminosity LHC. In Chapter 2, I will go into further detail, outlining the science of vertex detectors, and the issues that we face. To make measurements of the charge collection distance in diamond, I assembled a characterization station for prototype solid state detectors, which I will elaborate on in Chapter 3. In Chapter 4, I will outline the experimental measurements that I performed to measure the charge collection in diamond, and I will present my findings in Chapter 5. Finally, in Chapter 6 I will present my conclusions and outline possible paths for further research.

1.1 The LHC

The LHC is the highest-energy and largest particle accelerator in the world [2]. The LHC straddles the Franco-Swiss border near Geneva, Switzerland, at the European Organization for Nuclear Research (CERN). The primary objective for the LHC is to address fundamental questions about the Standard Model, which describes how elementary particles, like quarks and electrons, interact.

The LHC is situated in a tunnel 27 kilometers (17 miles) in circumference at a

depth of up to 175 meters (574 feet) below the surface. The LHC is designed to collide opposing beams of protons at energies up to 7 TeV per nucleon. Additionally, the LHC is also capable of accelerating lead nucleons at an energy of 574 TeV for heavy ion experiments. As illustrated in Figure 1.1, the LHC has four primary detectors. These detectors are ATLAS, CMS, LHCb and ALICE. My research is primarily concerned with a possible upgrade to the vertex detectors in ATLAS, a general proton-proton collision detector.

Figure 1.1: An aerial photograph of the location of the LHC on the Franco-Swiss boarder overlaid with a map of the LHC and its primary detectors, ALICE, ATLAS, CMS and the LHCb. The LHC includes a tunnel 27 km in circumference at a depth of up to 175 meters below the surface.

1.2 ATLAS

ATLAS, short for A Toroidal LHC Apparatus, is a general purpose detector that is set at one of the intersection points where proton-proton interactions occur. The primary goal of ATLAS is to look for new physics such as the mechanism for the origin of mass and the possible existence of extra dimensions [3]. As illustrated in Figure 1.2, ATLAS is a cylindrical detector 44 m (144 ft) in length and 25 m (82 ft) tall. The beam line is oriented along the long axis of the cylinder. The protons enter the detector along the beam line at opposing ends. The packets of protons then meet at the center of the detector where they collide, creating showers of particles that travel through the detector.

In order to reconstruct the particle paths and measure the energies, several different types of sensors are situated around the beam line. These detectors include calorimeters, used to measure the energy of the produced particles, muon detectors, which detect produced muons, and tracking detectors. The tracking detectors are embedded in a strong magnetic field that curves the particles' trajectories as they pass through ATLAS. This is a way to measure the charge and momenta of the particles. The tracking system also includes the vertex detector.
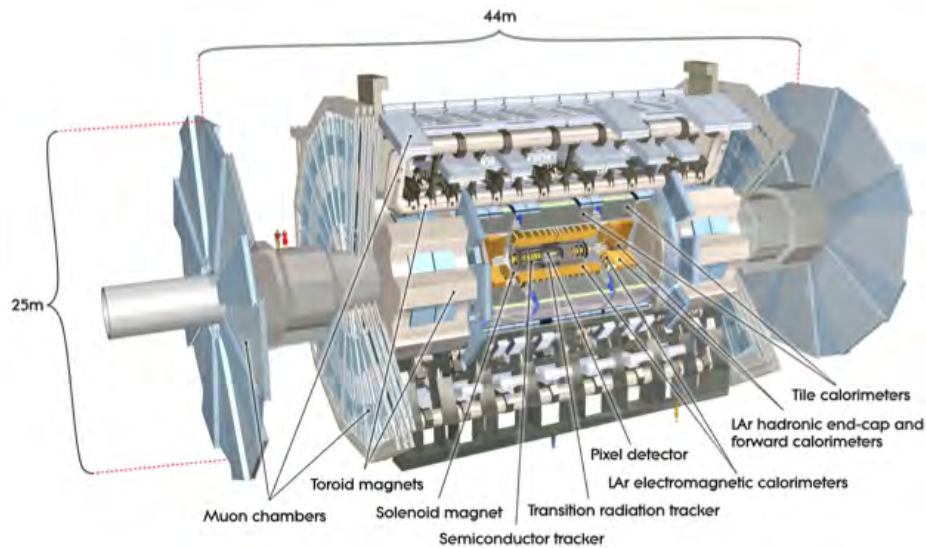
Figure 1.2: A cut-away view of the ATLAS detector. The detector is 44 m in length and 25 m tall. The proton beams enter the detector at opposite ends along the axis of the detector, then collide at the center of the detector, producing a shower of particles that pass through the various components. The research presented in this thesis is primarily concerned with the vertex detector which is labeled as "Pixel Detector" here. Note the people for scale in red at upper left.

1.3 Vertex Detectors

Vertex detectors, which are implemented in ATLAS as pixel detectors, are used to determine the initial trajectories of particles created in proton-proton collisions. These detectors are located in the inner detector of ATLAS in three layers at 50.5 mm, 88.5 mm and 122.5 mm radially outward from the center of the beam line, and on disks perpendicular to the beam line [3]. Vertex detectors sense when a charged particle passes through them by measuring the deposited charge left by the detector. As a charged particle passes through a vertex detector, it excites electrons in the valence band into the conduction band. Because an electric field is applied across the vertex detector, the charge migrates to electrodes where it is measured. Chapter 2 will cover in greater detail on how vertex detectors work and the issues that existing silicon detectors in ATLAS face.

1.4 High-Luminosity LHC

While the LHC is currently supplying important experimental results, there are plans to upgrade the luminosity of the accelerator over the course of the next decade [1]. This upgrade will increase the luminosity of the beam by a factor of 10, from the

current 10^{34}cm^{-2}s^{-1} to 10^{35}cm^{-2}s^{-1}. The primary motivation for this upgrade is to increase statistics for rare events, allowing for smaller uncertainties in discoveries made at the LHC.
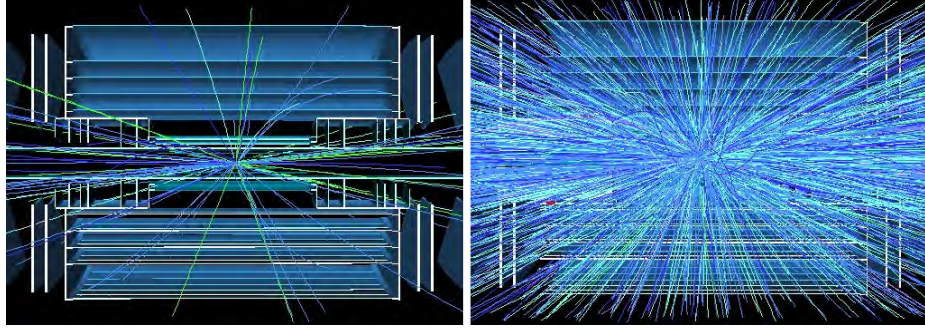
Figure 1.3: On the left is a simulation of particle tracks generated when two proton bunches collide at current luminosity. On the right is a simulation of the particle tracks generated after the luminosity upgrade. Figure adapted from [4].

While the upgrade in the luminosity will increase statistics and decrease uncertainties, it will also increase the fluence, or number of particles that are generated in proton-proton collisions. As Figure 1.3 illustrates, the increase from the current luminosity to a luminosity of 10^{35}cm^{-2}s^{-1} will result in many more particles passing through the detector. This increase in fluence across the detectors will lead to greater damage to the detectors. This damage, in turn will lower the signal-to-noise ratio of the detectors and will require replacing the vertex detectors over time. My interest is in measuring the charge collected by artificial diamond, which has a higher radiation hardness, or resistance to damage caused by radiation, and could potentially have a longer usable lifetime under the increased radiation environment at the High-Luminosity LHC.

Chapter 2

Diamond Vertex Detectors

The CERN RD-42 collaboration is interested in the potential of replacing the current silicon detectors with more robust diamond detectors. One figure of merit of the diamond detectors is their charge collection distance, which I set out to measure for this thesis. Before I explain how I performed this measurement, however, I must first describe how vertex detectors work, and why diamond could be a more suitable detector medium than silicon.

2.1 Vertex Detectors

Vertex detectors measure the creation of electron-hole pairs left behind by a charged particle when it passes through the detector. This process is shown in Figure 2.1. When a charged particle, such as a $\pi^{\pm}$ or a β particle, passes through the material, it imparts enough energy for electrons in the valence band to transition into the conducting band. When this occurs, the electron leaves a positively charged hole in its place. Because an electric field is applied across the junction, the electrons and holes travel in opposite directions, responding to the sign of the electric field, creating an electric current. This current is then picked up by electronics attached to the vertex detector and transmitted for further analysis.

In ATLAS, there are three concentric layers of vertex detectors surrounding the beam line, at radial distances of 50.5 mm, 88.5 mm and 122.5 mm from the axis of the detector and at disks perpendicular to the beam line [3]. These detectors are used to determine the location of vertices, the points at which a particle decays into daughter particles. A knowledge of where the decays occur is important to reconstruct the tracks of particles produced in proton-proton collisions. From these reconstructions different decay processes may be analyzed, giving new insight into the processes which govern the constituents of matter.

As illustrated in Figure 2.2, multiple layers of vertex detectors can be used to detect the daughter particles of a decay and reconstruct their trajectories. To begin this reconstruction, the location and time at which a particle passes through each layer
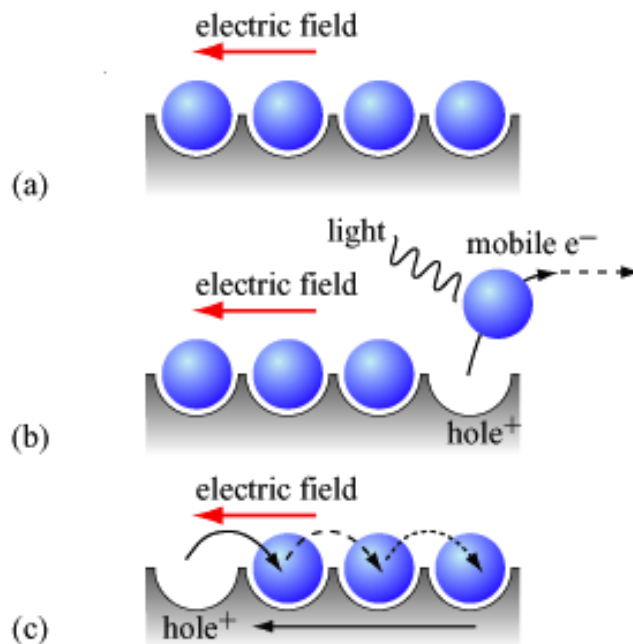
Figure 2.1: The theoretical model for the production and transmission of electron-hole pairs is presented. In **(a)** an external electric field has no affect on the electrons, blue spheres, because they are locked in the valence band. When an ionizing particle, in the case of **(b)** a photon, interacts with an electron, it imparts on it enough energy to move into the conduction band, leaving a positively charged hole in its place. This hole and electron, **(c)**, are then free to move in response to the electric field.

is recorded. This information is then used with momentum and energy conservation to reconstruct the trajectories of the tracks of particles generated in a collision event and determine the location of vertices. This information is then analyzed for information pertaining to rare decays or events that point to new physics.

While the vertex detectors are designed to track charged particles, this process also leads to detectors becoming damaged. Because of the high number of proton-proton collisions occurring at the LHC, ATLAS is in a high radiation environment, and all of its components are exposed to very high amounts of ionizing and nonionizing radiation. This creates defects leading to a decrease in the quality of the detector. There are two major possible defects that radiation can leave in a vertex detector: vacancy defects and interstitial defects. These are illustrated in Figure 2.3.

Vacancy defects can occur when radiation imparts enough energy to an atom to physically remove the atom from the crystal lattice. When this process occurs, it leaves a vacancy in the lattice that traps charges and prevents them from drifting when an external electric field is applied to the crystal. As a result, the measured amount of charge collected by the sample is lowered, and the detector loses efficiency.
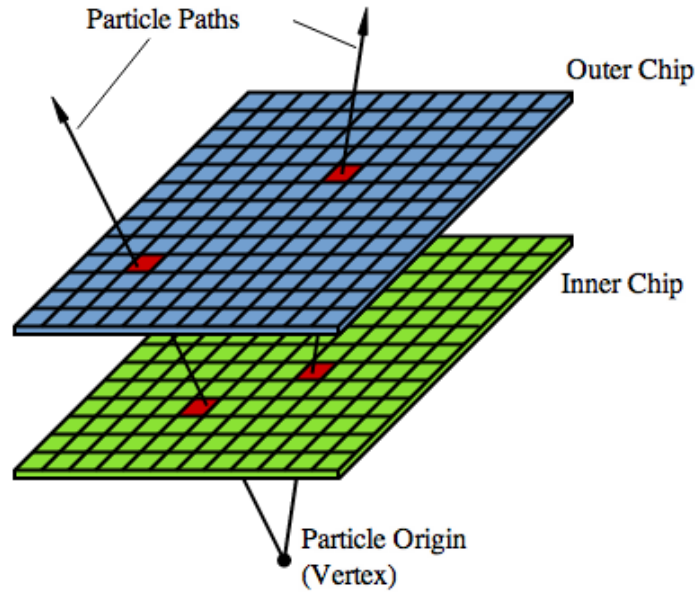
Figure 2.2: Multiple layers of vertex detectors can be used to reconstruct a particles trajectory. When a particle decays, it produces multiple daughter particles that then pass through the inner and outer chip layers. These layers each locate where the particle passed through the layer, which can then be used by software to reconstruct the particle's trajectory, and determine the location of the point of decay.
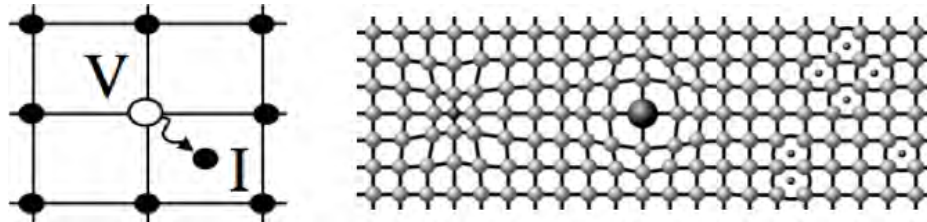
Figure 2.3: Two most common types of defects that can occur from radiation damage are shown. In the figure on the left, a charged particle has knocked an atom out of its place in the crystal lattice. This creates a vacancy, labeled **V**, that draws charge towards it. Another type of defect is interstitial, which is an atom in the wrong location of the lattice, such as **I** on the left, or impurities that change the electric properties of the lattice, such as those shown on the right.

The second type of defect, the interstitial defect, is actually a class of different types of defects, several of which are illustrated in Figure 2.3. An interstitial defect occurs when an atom is located at a point in the crystal lattice at which it does not belong. If an atom is knocked out of its position by a radiation event and creates a vacancy, the atom can also travel to some other location in the lattice. When this occurs, the atom changes the electric nature of the crystal lattice in the new location,

and can trap either holes or electrons, or hinder their travel when they respond to an electric field. As a result, the amount of measured charge decreases, and the accuracy of the detector falls. Other types of interstitial defects include atoms that replace the atoms in the crystal lattice, and thus alter the electric nature of the lattice. This second type of interstitial defect can occur during the manufacturing process.
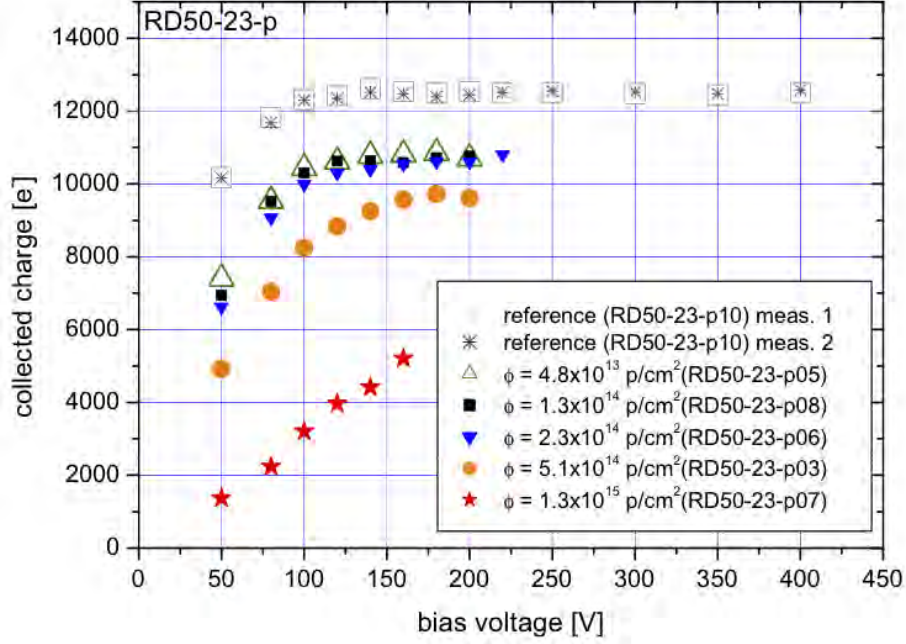
Figure 2.4: The amount of charge collected, in e^-, for silicon sensors is plotted as a function of bias voltage across the sample, in V. With increasing fluence the amount of charge that can be collected decreases. This is the result of damage done to the silicon detector by the radiation. Figure adapted from [5]

Damage to silicon detectors by irradiation has been well documented and is a major concern for the upgrade to the High-Luminosity LHC [1]. As illustrated in Figure 2.4, the charge collected by silicon detectors declines with increasing incident fluence. Here the maximum amount of charge collected declines to over fifty percent after the silicon detector is irradiated by $1.3 \times 10^{15} \mathrm{p/cm^2}$. Over the course of a decade, the vertex detectors in ATLAS and other detectors will be exposed to high levels of radiation, and undergo much damage. As a result, several possible candidates for a replacement detector medium have been purposed. These possible detector mediums include 3D silicon detectors [6], and diamond [7].

2.2 Diamond as a Detector Medium

Research into using diamond as a detector medium is spearheaded by the RD-42 collaboration, an international collaboration based at CERN to investigate the properties of diamonds that are relevant to particle detectors [7]. Diamond as a detector medium is of special interest because it is resistant to physical damage and has a high radiation hardness [8], where radiation hardness is resistance to damage caused by incident radiation. Diamond has a higher radiation hardness than silicon because the carbon atoms in diamond form a stronger chemical bonds than do silicon's. This tight crystal structure leads to greater resistance to the creation of vacancy and interstitial defects.

The diamonds that I used for this research are artificial polycrystalline diamonds 1 cm squared and 500 μm thick, created by the chemical vapor deposition (CVD) process. In the CVD process, a thin layer of diamond is built up by depositing carbon atoms from hydrocarbon gasses onto a suitable substrate at low pressures [9]. This process is able to create relatively pure diamond crystals that can be a few hundred microns thick, a thickness appropriate for vertex detectors.

To determine the value of diamond as a detector medium for vertex detectors, the charge collection distance of the material has to be measured. To do this, a charged particle is directed into the face of the detector, creating electron-hole pairs. Then an electric field is applied across the sample, which causes electron-hole pairs to separate, creating a signal that can be read out. This signal, called the collected charge, is proportional to the electric field applied to diamond and depends heavily on the amount of damage that previous irradiation of the sample has done. From this measurement of the collected charge, Q_{col}, the charge collection distance, d, may be determined [10]:

$$d \approx \frac{\langle Q_{col} \rangle}{36 e^-/\mu m} \tag{2.1}$$

Chapter 3

Characterization Station

In order to measure the charge collection distance of diamond, I needed to first build a characterization station that would enable me to make this measurement by using electrons from a radioactive source. The radioactive source is Sr-90 with an end-point energy of 2.28 MeV properly collimated to include only electrons with adequate energy to resemble minimum ionizing particles (MIPs). The collimator also serves to minimize multiple scattering effects in the detector by ensuring that most of the signals are recorded are from electrons which travel in a straight line [8]. This station is based on a design by Dr. Fred Hartjes, a researcher formerly with Nikhef, the Dutch national laboratory in Amsterdam. This station is composed of two parts, the preamplifier box, and the data acquisition (DAQ) box, that work in tandem with a personal computer to collect data on the charge collection in a prototype solid state detector.

To build the preamplifier and DAQ boxes, Dr. Hartjes directed me to his personal webpage that contains a highly detailed description of his characterization station, including mechanical drawings, data sheets, and operation manuals for many of the different components used throughout the station. His webpage may be accessed at [11], where a .zip file containing the plans and documentation for the characterization station may be found under **Documentation**: "Design plans of Nikhef characterisation station". Because the original plans for the station are readily available on the internet, I will focus on giving only a general outline of its use and operation, and specific changes that I personally made to the station during its construction.

3.1   Overview

The preamplifier box measures the current generated when a charged particle, supplied by a radiation source, travels through the sample. This signal is then amplified and shaped by Amptek A250 and Amptek A275 chips before being sent to the DAQ box. At the DAQ box, the signal is sampled by the computer where it is analyzed by a LabVIEW program. The DAQ box also contains the power supplies for the

preamplifier box, as well as pumps that supply a constant stream of air to the Peltier cooling system in the preamplifier box.
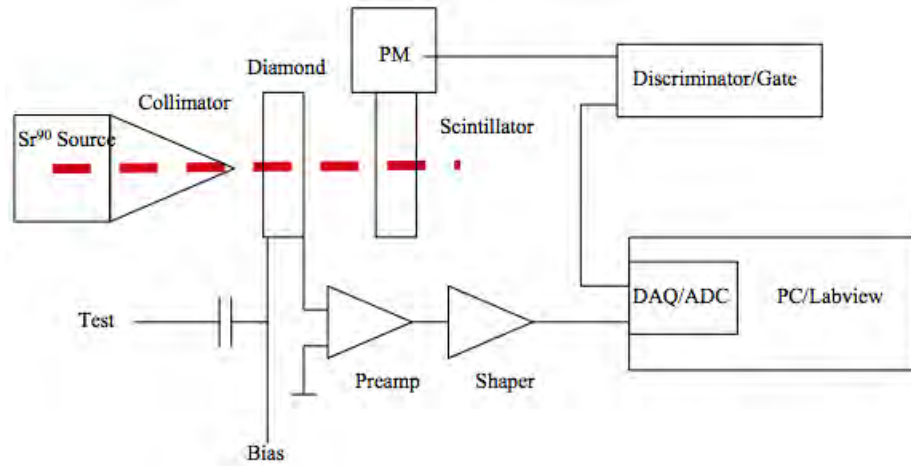
Figure 3.1: Here a schematic overview of the characterization station is given. The diamond sample is held between a Sr-90 source and a scintillator. When the Sr-90 emits a β particle, it travels through the diamond sample depositing charge and strikes the scintillator, which sends a signal to the discriminator. The charge deposited by the radiation event is then collected when a high electric field is applied across the diamond sample, generating a signal. This signal then travels through a preamplifier and shaper before reaching the DAQ station.

As illustrated in Figure 3.1, a collimated beam of β particles is directed from the Sr-90 source through the diamond sample. Sr-90 was chosen because the β particles produced are the closest the minimum ionizing energy. As the β particles pass through the diamond sample, they deposit charge, after which they strike the scintillator causing the PMT to trigger. This trigger is then sent to the discriminator and the DAQ box. The deposited charges are then measured by applying a voltage across the diamond sample, which generates a small signal. This signal is carried through preamplification and shaping chips before it travels to the DAQ box and PC where it is analyzed by LabVIEW software. To calibrate the station, described in greater detail in Section 4.1 below, a signal is sent into the characterization station at "Test" in Figure 3.1. This signal then passes through the preamplification and shaper chips before being read out by the DAQ box and PC. This process allows for the inherent noise and gain of the characterization station to be measured.

Figure 3.2 illustrates the box components before and after assembly. Some parts were purchased, while other components, such as the housing for the preamplifier box, were manufactured at the University of New Mexico.
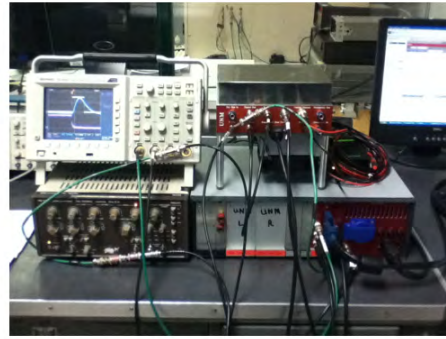
September 2011   March 2012

Figure 3.2: A side-by-side comparison of the components for the characterization station at the time of purchase and manufactured in September 2011, and in the fully assembled characterization station undergoing gain calibration in March 2012.

3.2   Preamplifier Box

The preamplifier box contains four major components: the PMT-scintillator assembly, the PCB boards used in shaping and amplifying the signal, the Peltier heat block, and the front plate with connectors for cables to the DAQ box. An overview of the preamplifier box is given in Figure 3.3.

The PMT-scintillator assembly is shown in Figure 3.4. For this assembly, a Hamamatsu PMT is connected to a miniature scintillator through a light guide encased in an aluminum tube, wrapped in mylar and shrink tube to prevent light leakage. The PMT-scintillator is then attached to an assembly that holds a collimator that is held at a constant 9.5 mm above the scintillator. This collimator has an aperture with a width of 0.6 mm that collimates the beam of β -particles that is emitted by a strontium-90 source. The location of the point where the collimated beam falls upon the sample may be adjusted by actuated stages in the X and Y directions.

The PCB boards are used to amplify the signal from the sample. There are four boards, a PC250 board, PC275 board, the main PCB board, and a smaller sample board connected to the main PCB. The main PCB supplies the voltage that creates an electric field across the sample. It then transfers the current that is generated when a charged particle from the strontium-90 source passes through the sample to the PC250 board. The PC250 board and PC275 board amplify the signal before transferring it to the connectors on the front panel, and then the DAQ box. The PC250 board contains an Amtek A250 chip, and at position C9 on the board, there is a test capacitor that is used in the gain calibration of the characterization station. The manufacturer of the board included a capacitor at this position, however, I replaced it with a larger capacitor that I measured to have a capacitance of 2.26 pF. How this capacitor is used in the gain calibration is discussed in the Section 4.1.

On the underside of the preamplifier box is a heat sink used to dissipate excessive

Figure 3.3: The interior of the preamplifier box showing the location of the components. The main components are: 1. the PMT-scintillator-collimator assembly 2. the airflow block that rests atop of the Peltier temperature control, 3. PC250 board and 4. PC275 board. The diamond samples are place under the collimator at 5.

heat. It is attached to a computer fan used for cooling. Above the heat block is a Peltier cooler attached to an aluminum circulation block. By adjusting the current supplied to the Peltier cooler, the temperature of the circulation block, and the air passing through it, may be adjusted so that the air passing over the sample is held at a constant desired temperature. The air passing through the circulation block is provided by two pumps located in the DAQ box. The temperature of the air passing through the circulation block is measured by two thermistors attached to the sample board, and by a Sensirion humidity and temperature detector.

There are eleven connectors on the faceplate of the housing block. There are three connectors for circulation, two that connect to the pumps in the DAQ box and a third which can be used to supply dry air. Also connecting to the DAQ box are BNC connectors for the Test-in, PM-pulse, Signal out and Vbias signals. Additionally, there is a high voltage connector and a 15 pin connector that carries the power for the fan and various other components. There are two special connectors, one for the Sensirion humidity detector, and another for the Peltier cooling block.

3.3   DAQ Box

In addition to housing the power supplies for the preamplifier box, the DAQ box serves as a bridge between the preamplifier box and the computer. As illustrated in

Figure 3.4: The PMT-scintillator assembly is shown. The PMT is located at the left, where it is connected to the housing of the collimator, top center, and the scintillator, center. The radiation source, Sr-90, is placed atop the collimator, which directs the beam of charged particles to the scintillator, after they have passed through the diamond.

Figure 3.5, the DAQ box holds five different power supplies. The first power supply is a high-voltage power supply that provides the bias voltage that the preamplifier box uses to generate an electric field across the samples. There is also a pair of 6V power supplies that convert AC to DC current. This current is then down regulated in the PM-Ctrl module to 5V and used to power the PMT. Finally there are two more 24V AC power supplies. One of these 24V powers the pumps, while the other is connected to the preamplifier box by the 15 pin D-connector, where it powers both the cooling fan and the chips on the PCB boards.

While Dr. Hartjes gave me many of the components for the DAQ box in their final, fully assembled form, I still needed to make some corrections and additions to the DAQ box before it would work properly.

The first set of adjustments that I performed was on the PM-Ctrl module. This module is the one that sits at the heart of the DAQ box and routes the various signals between the five different power supplies, the preamplifier box, the displays on the front panel of the DAQ box, and the computer running LabVIEW. The first adjustment that I made was to down regulate the voltage to the PMT. In Dr. Hartjes' original characterization station, he used an older PMT that ran off of a 12V power supply, while the PMT in my characterization station was only rated to 5V. To perform this down regulation, I replaced two resistors and added an additional transistor to change the voltage of the signal. Additionally, I added a new connector
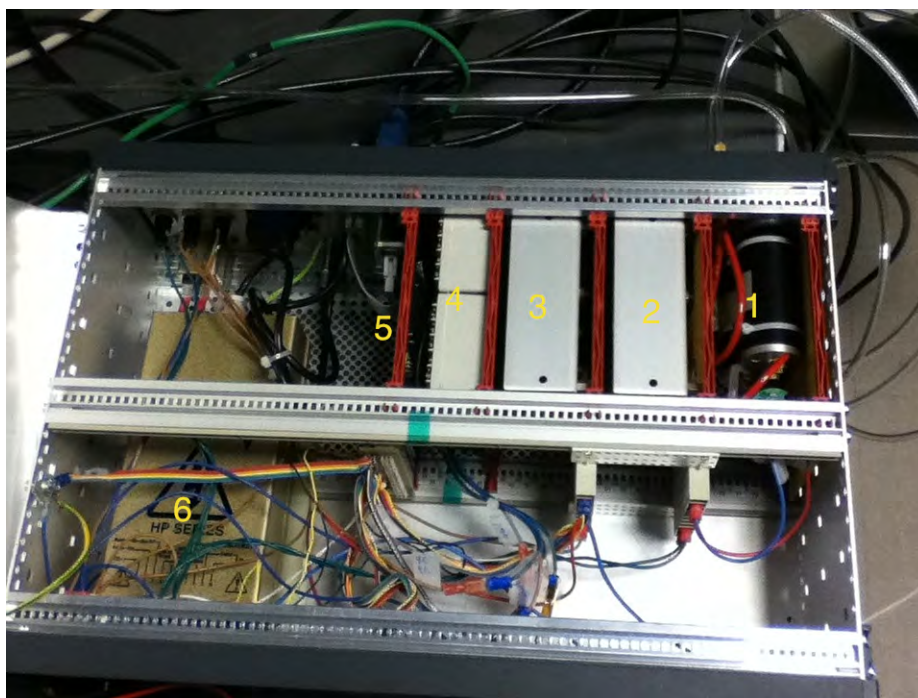
Figure 3.5: A photograph of the interior of the DAQ box. There are multiple components including: 1- the pumps that circulate the air inside of the preamplifier box. 2- the first 24 V power supply that powers the pump. 3- the second 24 V power supply that is fed into the preamplifier box. 4- the two 6 V power supplies that generate a DC current to power the PMT. 5- PM-Ctrl module that connects the various components together, and connects the DAQ box to both the computer and preamplifier box. 6- high-voltage power supply.

at the interface of this module and the rest of the DAQ box that replaced the ribbon cable his original plan called for with individual wires.

Because the characterization station that I borrowed from Dr. Hartjes was designed to run off of 220V, and not the 110V voltage that is standard in the United States, I adjusted the various components in my DAQ box accordingly. To make these adjustments, I changed the 24V and 6V power supplies so that they would work with the different AC power supplies. I redid the wiring throughout the DAQ box, removing the European style power outlet, and replacing it with an American style power outlet, and adjusting the wiring of the fuses, switches and power supplies accordingly.

The final difference between my version of the DAQ box, and Dr. Hartjes' original design was that I used a different high-voltage power supply. In his DAQ box, he used a power supply which uses ribbon wires to make electrical connections, while I used a power supply which does not. As a result, many of the connectors that the original design called for had to be replaced with other single-wire connections. To account

for these new connections, many of the ribbon wires from the PM-Ctrl module were either replaced or bound together before connecting to single wires. Because my power supply handles polarity differently from his, Martin added an op amp to the PM-Ctrl that alters the incoming signal so that both positive and negative polarities can be used.

3.4   LabVIEW DAQ and Analysis

The direct analysis of the data is performed by a series of LabVIEW VI's, or LabVIEW based software routines, written by Dr. Hartjes, and included with his description of the characterizations station at [11]. In addition to many subVI's, the primary VI's involved in the collection of data and its analysis are Meas6024E-upgrad.vi and Newana2.vi.

Meas6024E-upgrad.vi is primarily used in the calibration of the characterization station and the collection of data. The front panel of this VI is shown in Figure 3.6. This program measures the peak-to-peak voltage of the DAQ signal and creates a histogram of these data. In addition to the histogram, the program creates a .txt file containing the data to be analyzed by Newana2.vi. To calibrate the characterization station, the clock on the Meas6024E-upgrad.vi is set to "internal," and then a histogram with a gaussian distribution is generated from the measured values of the DAQ signal. This distribution is the inherent noise of the characterization station, and the mean of the distribution and its standard deviation are measured as a part of the calibration process, yielding the pedestal and noise respectively.

When Meas6024E-upgrad.vi is used to collect data, a .txt file containing the voltage per micron, number of events required for measurement, and destination for the output file is created, and then read by CCD6024-upgrad.vi. This second VI then steps up the voltage across the sample as specified and directs the Meas6024E-upgrad.vi to measure the peak-to-peak value of the DAQ signal, generating a histogram of the results and .txt files containing the information from the histogram. When this histogram is created, as illustrated in Figure 3.6, it features two different distributions, the gaussian noise distribution mentioned above, and a second that follows a Landau distribution, representing the amount of charge collected by the sample when a β particle from the Sr-90 source passes through it. To determine the amount of charge collected, the output files are then read and analyzed by Newana2.vi.

After Meas6024E-upgrad.vi writes the data files, Newana2.vi reads them. Newana2.vi then fits a convoluted distribution to the data using the Levenberg-Marquardt fitting algorithm as described in [12]. Briefly, the VI creates a convolution of the two functions, $g(x)$ and $f(x)$, given by [13] as:

$$f * g = \frac{1}{\sqrt{2\pi}} \int_{-\infty}^{\infty} g(y)f(x-y)dy. \tag{3.1}$$

Newana2.vi is then able to extract the two distributions from the data. The first

16
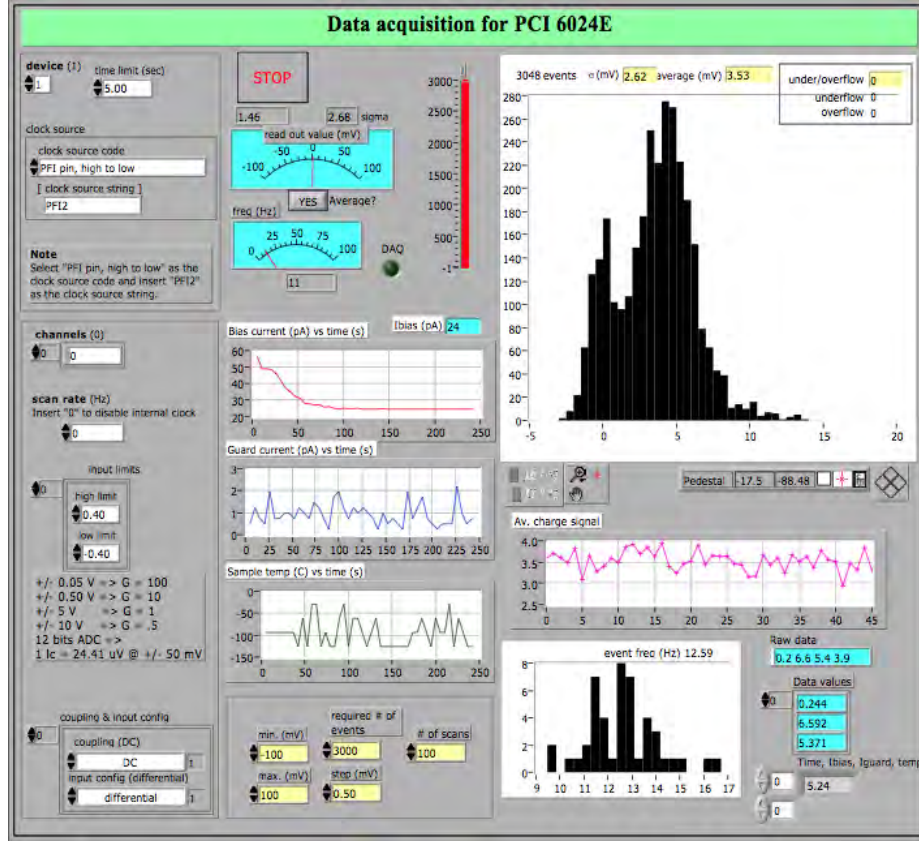
Figure 3.6: A screen capture of the Meas6024E-upgrad.vi that measures the peak-to-peak voltage and generates a histogram of the data. The parameters that control the data selection are the white boxes on the left, and the yellow boxes on the bottom. Note that in the histogram in the upper right there are two main peaks. The peak on the left represents the noise, while the larger peak on the right represents the signal from the characterization station.

distribution, as mentioned above, is the gaussian distributed noise. The second distribution follows a Landau distribution. This distribution describes a sharp increase followed by a steady decline and is characteristic of the fluctuations of energy loss of a charged particle as it passes through a thin layer of matter, such as silicon or diamond [14] [15]. One form of the distribution is given in Equation 3.2, where $p(x)$ is the probability distribution for a parameter x:

$$p(x) = \frac{1}{\pi} \int_0^\infty e^{-t\ln t - xt} \sin \pi t \, dt. \tag{3.2}$$

To determine this distribution, Newana2.vi begins with an empirical approximation, L, that is a function of the height parameter of the Landau distribution, p_4, as given in [11]:

$$L = p_4 \sqrt{e^{G+e^{-G}}}. \tag{3.3}$$

Here G, which is a function of the most probable value of the distribution, p_1, the width parameter of the distribution $b \approx (rms/2.221)$, and the measured charge, x, is defined as:

$$G = \frac{x - p_1}{b}. \tag{3.4}$$

After performing this fit, the independent parameters, p_1 and b are read out on the front panel of Newana2.vi, giving the most probable value and the variance of the Landau distribution respectively. The front panel of Newana2.vi is given in Figure 3.7, while a close up of the fit of the Landau and Gaussian distributions to the data is given in Figure 3.8. To assess the accuracy of these measured values, the mean squared error (MSE), for the Landau distribution is calculated by Newana2.vi and read out. When some sample data was analyzed by both Newana2.vi and ROOT, the software packages produced slightly different statistical calculations. In Newana2.vi, the most probable value for this distribution was determined to be 3.94 mV, while in ROOT it was 3.70. Also ROOT calculated a χ^2 value for its fit of 7.43, indicating that we can be fairly confident in the values of p_1 and b. A side-by-side comparison is given in Figure 3.9.
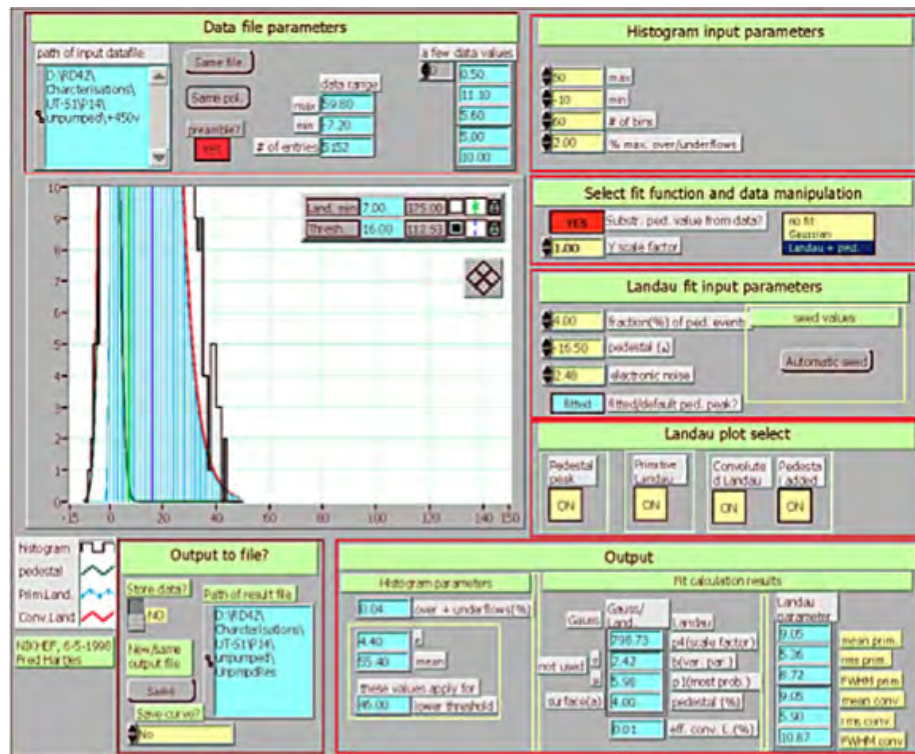
Figure 3.7: Newana2.vi is shown. The noise and pedestal values are entered into the yellow boxes on the center-right, and the fitted data are graphed on center-left. The parameters of these fits are then displayed in the blue boxes on the lower right.
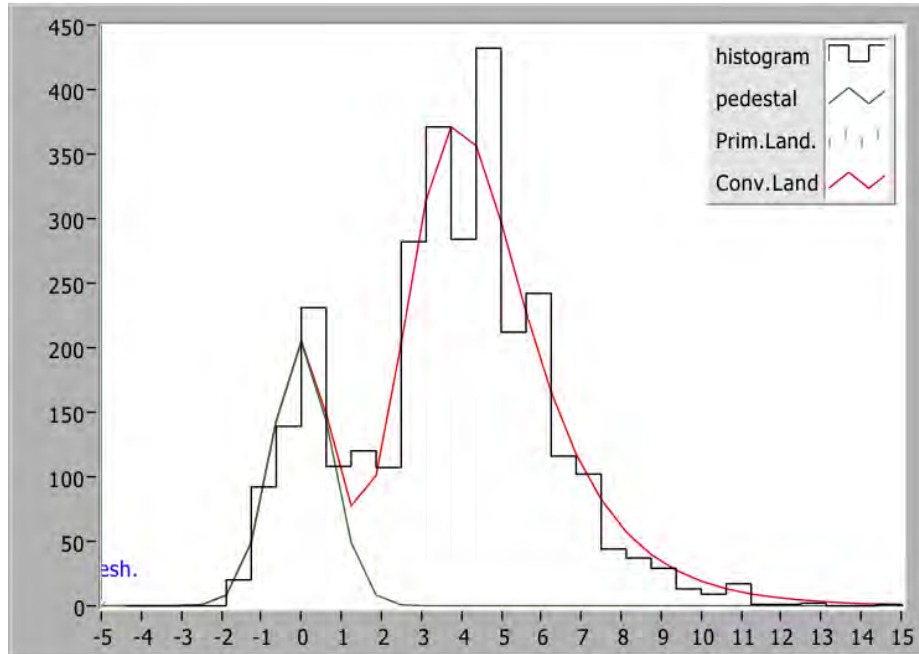
Figure 3.8: The output of the fitting process is presented. The solid black line represents the histogram of the raw data, the green line is the gaussian noise, the faint blue line is the Landau distribution, and the red line is the convolution of the gaussian and Landau distributions.
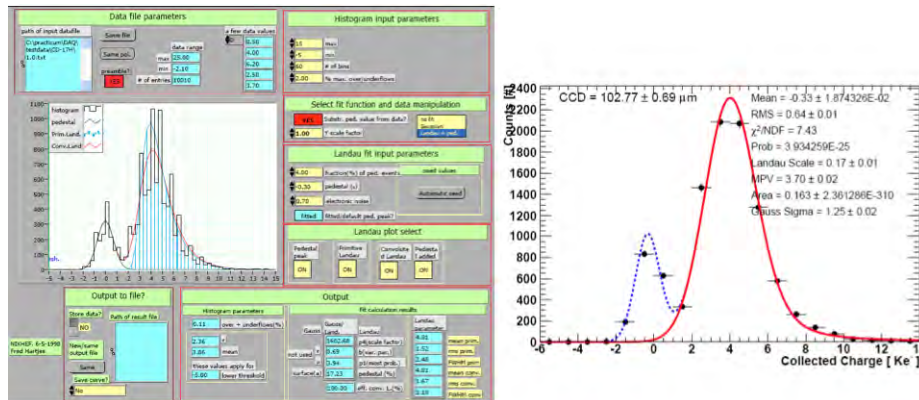
Figure 3.9: A side-by-side comparison between the Newana2.vi and ROOT analysis of a sample set of data. The Newana2.vi analysis determines a most probable value of 3.94 mV, while ROOT gives a value of 3.70 mV. The ROOT analysis has a χ^2 value of 7.43.

Chapter 4

Experimental Procedure

The experiment was performed on several different occasions. During October of 2011, Martin Hoeferkamp collected initial data on one of the diamond samples, CD-17, for the non-irradiated state on Dr. Hartjes' original characterization station. Then during December of that same year, many members of Dr. Seidel's research team, myself included, travelled to Los Alamos National Laboratory (LANL) to irradiate the diamond samples at LANSCE, the Los Alamos Neutron Science Center. This was done as a part of a larger international collaboration where multiple electronic systems and samples, including the CD-17 diamond, were irradiated with a total fluence of 2.74×10^{15} 800 MeV p/cm^2. Then in March of 2012, I collected data, as described below, for the irradiated CD-17 sample and the non-irradiated CD-68 diamond sample.

4.1 Calibration

The characterization station must be calibrated before taking data. This calibration generates the gain, noise, and pedestal values.

The gain calibration depends on the test capacitor, C9, on the PC 250 board in the preamplifier box. As mentioned in section 3.2, the value of this capacitor was measured to be 2.26 pF; additionally there is some parasitic capacitance in the board, given as 0.11 pF [11]. A Philips PM 5786 pulse generator was used, with attenuation, to create a square-wave signal of a few mV peak-to-peak that was then measured on a Tektronix TDS 3054C oscilloscope. A test pulse was supplied, at a variable voltage of V_T, to the characterization station. From the characterization station, a gaussian signal with a mean of $\bar{x}$ and variance σ was measured using the built-in Meas6024E-upgrad.vi in LabVIEW. These values are summarized in Table 4.1.

To determine the gain from these values of V_T, $\bar{x}$ and σ, the test voltage had to be first converted from mV into charge. To do this, the test voltage is multiplied by the sum of the test capacitance, C_T measured at 2.26 pF, and the parasitic capacitance, C_P given as 0.11 pF. This value in Coulombs is then converted into number of electrons

$V_T(mV)$	$\bar{x}(mV)$	$\sigma(mV)$
1.04	30.66	0.81
1.52	43.58	0.81
2.00	57.46	0.81
2.48	69.60	0.82
3.04	85.76	0.83

Table 4.1: The values of the gain calibration are represented. In the first column are the input voltages, V_T. In the second and third columns are the mean $\bar{x}$ and variance σ of the output voltages. All values are given in mV.

giving the number of charges input, $q(e^-)$, as shown in Equation 4.1.

$$q(e^-) = \frac{(C_T + C_P)V_T}{1.602 \times 10^{-19} C/e^-} \tag{4.1}$$

I plotted the values of the output voltage, $\bar{x}$, as a function of the input charges, $q(e^-)$ in a scatter plot. I then used the method of least-squares fit for a line, as described in [16], and the MATLAB functions of polyfit and polyval, to determine the best fit line, as described in [17]. These data are presented in Figure 4.1. The reciprocal of the slope of this line is the gain, G, and was found to be $534e^-$/mV. A similar process was used for Dr. Hartjes' original characterization station, and his station was found to have a gain of $446e^-$/mV.

To measure the noise and pedestal, I connected the Supply, Bias, Test In and Signal ports on the preamplifier box to the DAQ box. In the Meas6024E-upgrad.vi, I set the clock source to "internal" and the scan rate to 75 Hz and ran the VI for 3,000 events for ten different runs. This process generated a gaussian distributed histogram. Using the LabVIEW software, I measured the mean of this distribution, $\bar{x}$, and its variance, σ, both in millivolts. This was done in the same manner as when I measured the gain. These values are given in Table 4.2. The average values of $\bar{x}$ and σ were then used as the pedestal and noise when analyzing the data, as described in Chapter 5.

I then measured the noise and pedestal values for differing conditions for the characterization station. These measurements are summarized in Table 4.3. I measured a control noise and pedestal value of -1.96 ± 0.68mV with 3000 events and 30 minute warmup at 22.0^oC and 22% relative humidity. I then varied each of these parameters individually. I made measurements for differing warmup times from 0 minutes to 30 minutes. I then varied the number of events over which I measured the noise and gain from 100 events to 10,000 events. I then adjusted the environmental conditions by first pumping N_2 gas into the characterization station to achieve a relative humidity of 0.10 %, and I changed the temperature to 17.0^oC and 27.0^oC. The greatest difference among these measurements occurred when I measured the noise and pedestal with
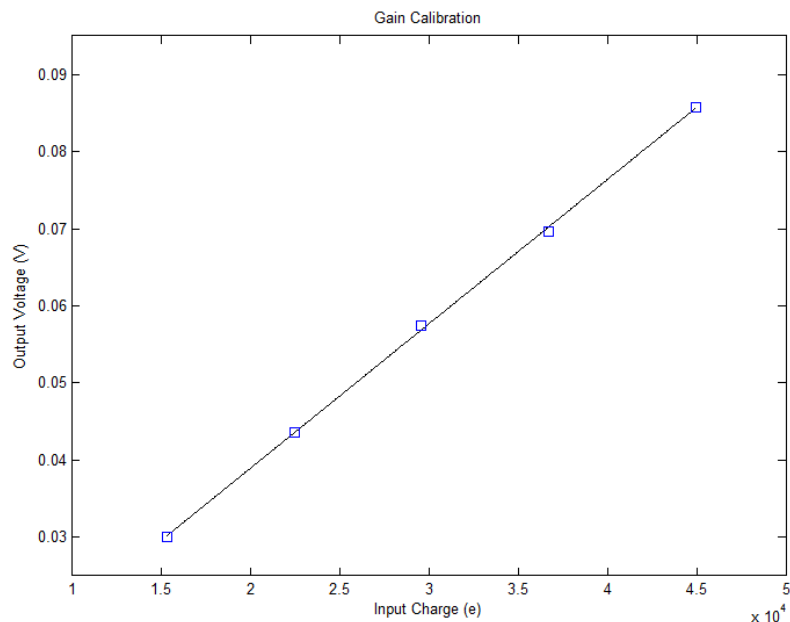
Figure 4.1: The output voltage, $\bar{x}$ measured in V, is plotted as a function of the input charge, $q(e^-)$, measured in electrons. By using the method of least-squares fitting, and the polyfit and polyval functions in MATLAB, it was determined that the characterization station has a gain $G = 534e^-/\text{mV}$, by calculating the inverse of the slope of the fitted line.

Run Number	$\bar{x}(mV)$	$\sigma(mV)$
1	-1.96	0.59
2	-1.99	0.60
3	-1.99	0.61
4	-2.00	0.60
5	-1.99	0.59
6	-1.99	0.59
7	-1.97	0.60
8	-2.00	0.59
9	-2.00	0.59
10	-1.99	0.61
Average Values	-1.99	0.60

Table 4.2: Noise and pedestal value calibration data.

only 100 events, giving a value of -2.06 ± 0.69mV. As Table 4.3 illustrates, the noise and pedestal values do not vary significantly under differing experimental conditions.

Condition	$\bar{x}(mV)$	$\sigma(mV)$
Control	-1.99	0.68
0 min warmup	-2.02	0.69
10 min	-1.99	0.69
20 min	-1.99	0.68
30 min	-2.02	0.68
100 events	-2.06	0.69
500 events	-2.00	0.70
1000 events	-2.01	0.69
10,00 events	-1.99	0.68
0.10 % RH	-2.01	0.69
17.0^oC	-1.98	0.71
27.0^oC	-1.96	0.72

Table 4.3: Noise and pedestal values for differing conditions. With the exception of the altered parameter, all measurements were identical to the control.

4.2   Preparing the Diamond

Two different diamond samples were used, diamonds CD-17 and CD-68. Both of these diamonds are 500 microns thick approximately 1 cm × 1 cm.

Prior to taking any data the diamonds must be pumped to recreate the conditions in ATLAS. To pump the diamond samples, the same Sr-90 sources used to collect data is placed on top of the sample and left for a number of hours. The samples do not have sufficient charge in the un-pumped state to carry a signal when an electric field is applied across them. Pumping the samples allows for the diamond to capture charges by saturating deep traps [18], essentially filling vacancies were electrons were removed in the irradiation process.

One of the diamonds, CD-17, was irradiated at LANSCE in December of 2011 over the course of several day, while the other sample CD-68 was not. At LANSCE, bunches of protons were fired through the the diamond, perpendicular to the square face. In total, the sample was irradiated with a total fluence of 2.74×10^{15} 800 MeV p/cm^2.

4.3   Experiment

As mentioned above, the data used for analysis was collected on two separate occasions. In October of 2011 one of my mentors, Martin Hoeferkamp, gathered data on the non-irradiated CD-17 sample using the characterization station that we borrowed from Dr. Hartjes. To do this, he pumped the diamond for 25 hours. Then he placed the diamond into the preamplifier box, and placed the Sr-90 above the collimator so

that the collimated beam of β particles would pass through the sample, and strike the scintillator-PMT. Then he passed various electric fields across the sample. These fields began at 0V, and moved up to +500 V in 100 V steps, at which point the voltage was stepped down to -500 V. After reaching -500 V, the voltage was then ramped up to 0 V, for a total of twenty-one sets of data. This pattern is necessary to detect any discrepancies that depend on the polarity of the electric field. For each of these voltages, the data were collected for 3000 radiation events.

In March of 2012, I followed the above procedure for the irradiated CD-17 sample, and the non-irradiated CD-68 sample. Prior to collecting the data, however, I pumped the CD-68 sample for a total of twenty-two hours, and the irradiated CD-17 sample for eighteen hours. I then measured the collected charge as a function of bias voltage across the sample, in the same manner as described above. To determine the effect of pumping on the CD-17 sample, I then further pumped the sample and repeated the characterization at forty-eight and seventy-two hours of pumping. This additional pumping was necessary to determine the effect pumping has on charge collection. It has been suggested that after irradiation diamond samples require longer pumping times [19]. The results from all five of these characterizations are summarized in Chapter 5.

Chapter 5

Experimental Outcomes

I measured the charge collection using the characterization station for a range of bias voltages across the diamond samples. This data was collected using the Meas6024E-upgrad.vi and generated in the form a histogram.

I ran these data files through the Newana2.vi program to determine the most probable value for the Landau distribution and its variance. I converted these values, which were measured in mV, into number of electrons using the gain values calculated above, $G = 534e^-/\text{mV}$ for my characterization station and $G = 446e^-/\text{mV}$ for Dr. Hartjes' station. These two different gain values are necessary for the CD-17 diamond sample, which was characterized on Dr. Hartjes' station prior to irradiation, and then characterized again on my station after the irradiation. The results of these experiments and data analysis are summarized in Figures 5.1 to 5.3. Throughout each of these data sets, with increasing bias voltage, the amount of collected charge increases. As the bias voltage then decreases, a hysteresis effect develops resulting in a lower amount of collected charge at each voltage. This effect is also present when the bias voltage increases from -500 V to 0 V.

To facilitate a comparison between the various samples, the most probable values for CD-68 and CD-17 before and after irradiation are plotted in Figure 5.4. From this figure, it is clear that irradiation did have an effect on the CD-17 sample. Prior to irradiation, the sample showed a peak charge collection of $1920 \pm 18 \ e^-$ when a bias voltage of 500 V, 1.0 V/μm, was placed across the sample. After irradiation this sample only collected $950 \pm 16 \ e^-$ for the same bias voltage, a decrease of 51 %. In comparison, the CD-68 sample collected $3870 \pm 32 \ e^-$ when measured at the same bias voltage.

The collected charge for the different pumping times for CD-17 is plotted in Figure 5.5. It is clear that there is a distinction between the non-irradiated and irradiated sample. For a bias voltage of 500 V, 1.0 V/μm, across the sample, the non-irradiated state showed a collected charge of $1920 \pm 18 \ e^-$. The irradiated sample showed a collected charge of $950 \pm 16 \ e^-$ when pumped for eighteen hours, $1090 \pm 19 \ e^-$ when pumped for forty-eight hours, and $1160 \pm 19 \ e^-$ when pumped for seventy-two hours.
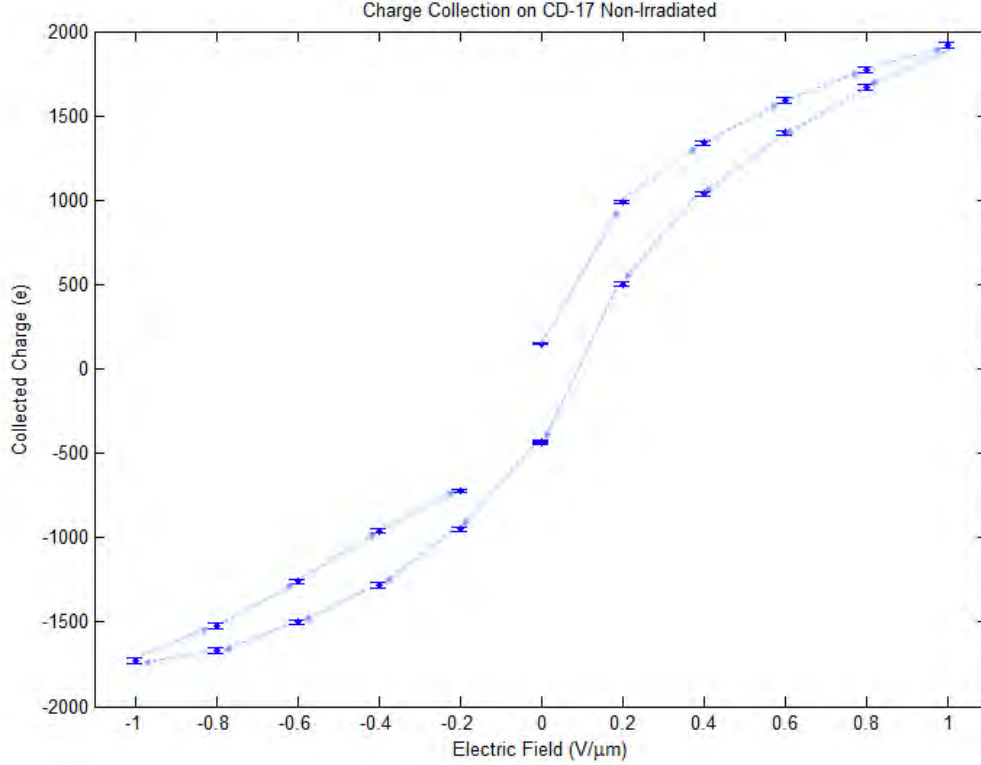
Figure 5.1: The collected charge, in number of electrons, is plotted as a function of the bias electric field across the diamond, in $V/\mu m$ for the diamond sample CD-17 prior to irradiation at LANCSE. To collect these data, the bias field was set first at 0V, and ramped up to +500 V in 100V steps after which it was ramped down to -500 V, before being brought back to 0 V.

This corresponds to an increase of 140 e^- when going from eighteen to forty-eight hours, an increase of 14.7 percent, and an increase of 210 e^-, 22.1 percent, when pumped for seventy-two hours. This values are summarized in Table 5.1. This trend is the case for all bias voltages except 200 V and 300 V, where some values for the longer pumping times are lower than the eighteen hour pumping time.

As illustrated in Figure 5.6, there is a difference between the amount of collected charge measured depending on whether the bias voltage is increasing or decreasing. The amount of collected charge is higher for an increasing bias voltage than for a decreasing voltage. For a bias voltage of 400 V, 0.8 $V/\mu m$, the amount of collected charge on CD-68 is 3510 $\pm$ 30 e^- for increasing voltage and 3220 $\pm$ 29 e^- for decreasing. The measurement curve in Figure 5.6 shows a hysteresis because of the capacitance and high resistivity of diamond [10]. When diamond is used as a detector medium, it is customary to increase the electric field across the sample to 1 $V/\mu m$
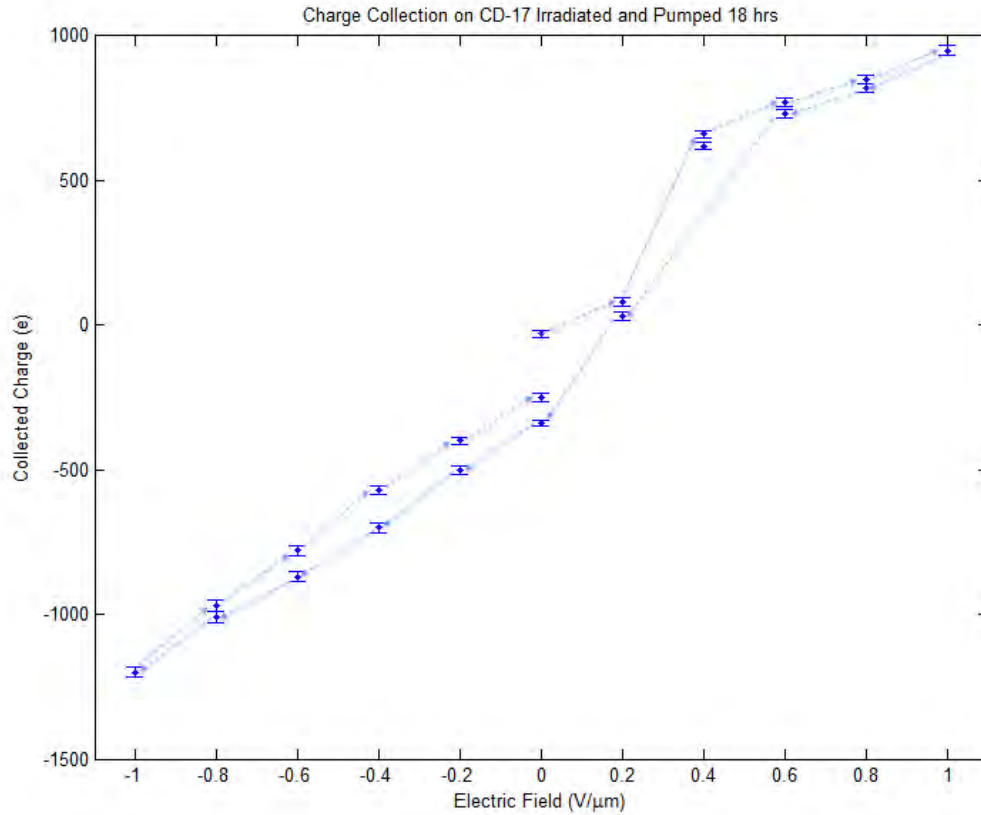
Figure 5.2: The collected charge, in number of electrons, is plotted as a function of the bias electric field across the diamond, in V/μm for the diamond sample CD-17 after it was irradiated at LANCSE to a net fluence of 2.74×10^{15} 800 MeV p/cm^2. To collect these data, the bias field was first set at 0V, and ramped up to +500 V in 100V steps after which it was ramped down to -500 V, before being brought back to 0 V.

without passing it.

From the measured values of the charge collected, the charge collection distance for CD-68 and CD-17 may be determined by Equation 2.1. CD-68 has a peak charge collection distance of 107.4 ± 0.9 μm, which occurs at a bias voltage of +500V. Without irradiation, CD-17 has a peak charge collection distance of 53.4 ± 0.5 μm, also for a bias voltage of +500V. After irradiation, the charge collection distance at the same bias voltage is 26.4 ± 0.5 μm when pumped for eighteen hours, 28.9 ± 0.5 μm when pumped for forty-eight hours, and 32.2 ± 0.5 μm when pumped for seventy-two hours.
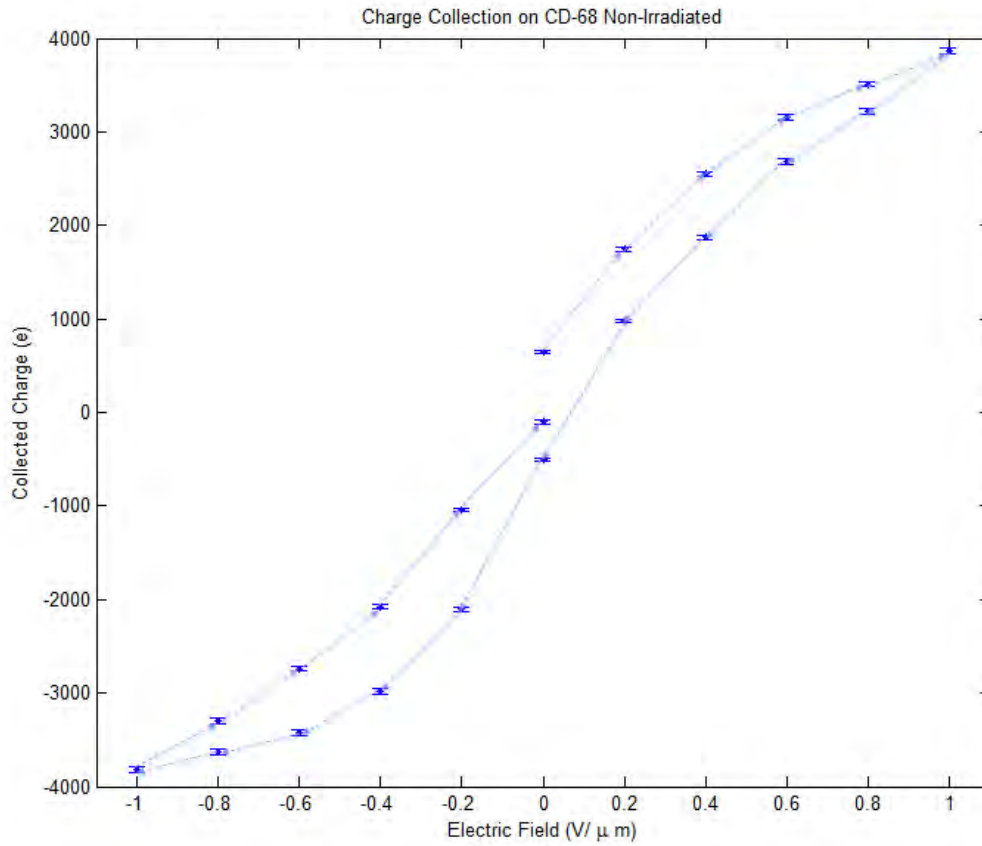
Figure 5.3: The collected charge, in number of electrons, is plotted as a function of the bias electric field across the diamond, in V/μm for the diamond sample CD-68, which was not irradiated. To collect these data, the bias field was first set at 0V, and ramped up to +500 V in 100V steps after which it was ramped down to -500 V, before being brought back to 0 V.
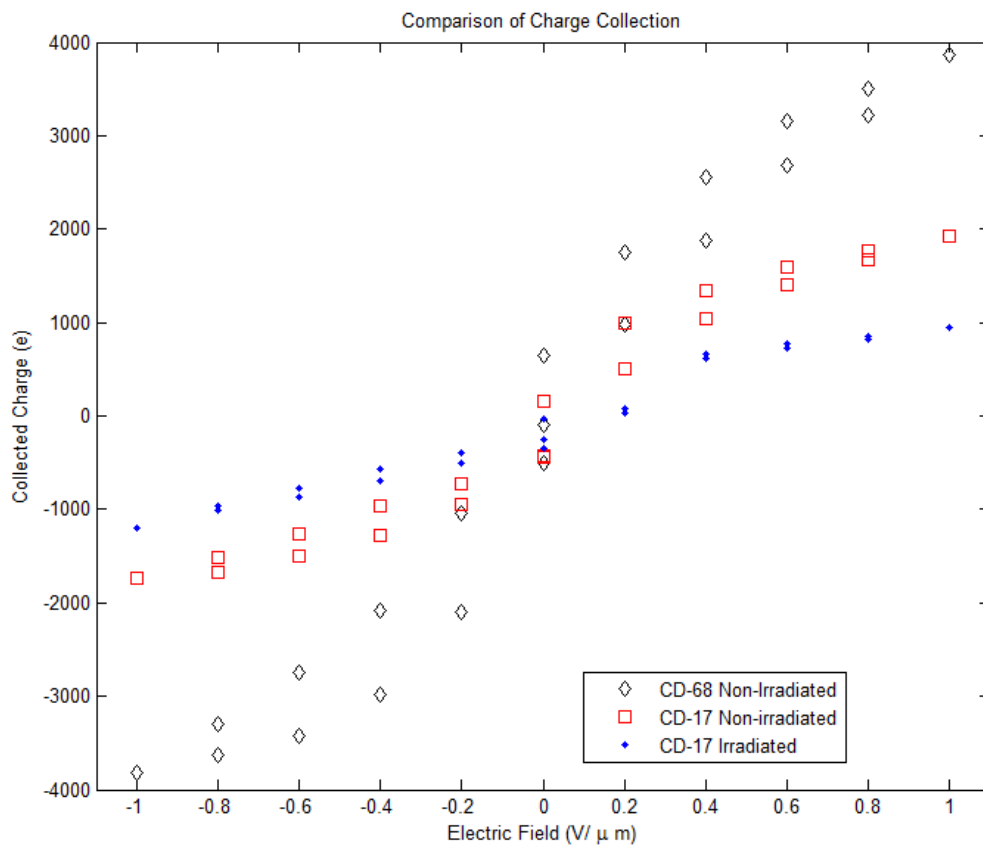
Figure 5.4: The most probable value for the number of collected charges, in number of electrons, is plotted as a function of bias voltage, in V/μm for all three diamond samples. Sample CD-68 is represented by the black diamonds, while the red squares and blue dots represent the non-irradiated and irradiated CD-17 sample, respectively. Note that the error bars for these data sets are smaller than the symbols used in the plot.

Sample (Pumping Time)	Charge Collection e^-	% of Non-irradiated	% Increase
Non-Irradiated (25 hrs.)	1920 ± 18	-	-
Irradiated (18 hrs.)	950 ± 16	49.5	-
Irradiated (48 hrs.)	1090 ± 19	56.8	14.7
Irradiated (72 hrs.)	1160 ± 19	60.4	22.1

Table 5.1: Charge collection for the CD-17 sample. The first row is the non-irradiated CD-17 sample and the last three rows are for the irradiated sample with pumping times in parentheses. The amount of charge is given in e^-. The % of Non-irradiated is the amount of charge collected as a percentage of the amount collected for the non-irradiated sample. The % Increase is the percentage increase of charge collected when compared to the irradiated sample pumped for 18 hours.
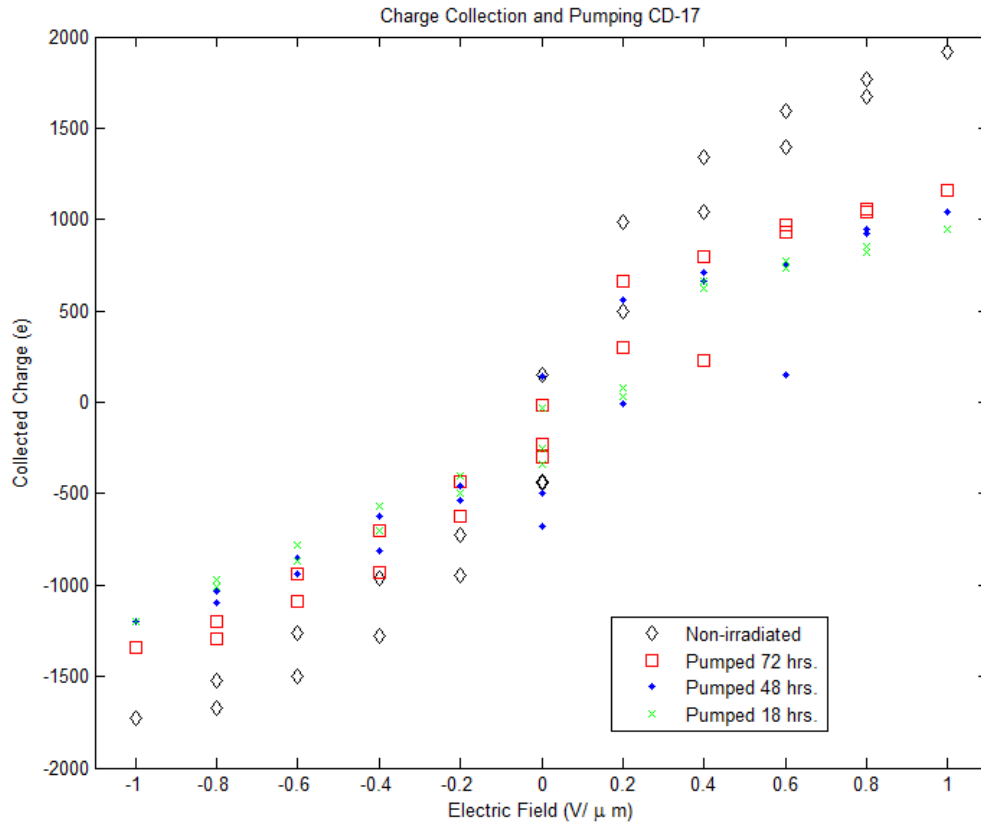
Figure 5.5: The most probable value for the number of collected charges, in number of electrons, is plotted as a function of bias voltage, in V/μm for CD-17 at different pumping states. The black diamonds represent the non-irradiated sample. The red squares is the irradiated sample after 72 hrs. pumping, the blue dots for 48 hrs. of pumping, and the green crosses for 18 hrs. of pumping. Note that the error bars for these data sets are smaller than the symbols used in the plot.
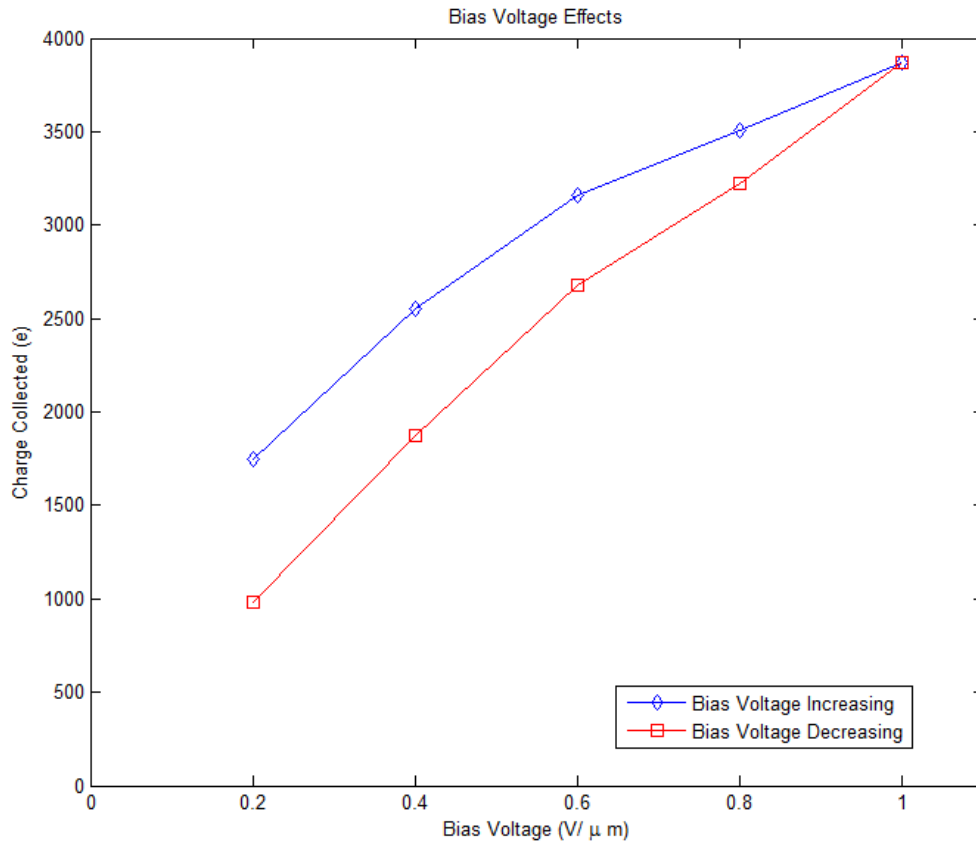
Figure 5.6: The hysteresis effects in the CD-68 sample. As the voltage increases, blue diamonds, the amount of charge collected increases, but as the charge decreases, red squares, the measured amount is smaller. Note that the error bars for these data sets are smaller than the symbols used in the plot.

Chapter 6

Conclusions

For this thesis, I measured the charge collection for diamond both before and after irradiation. To do this, I assembled a characterization station based on designs by Dr. Fred Hartjes formerly from Nikhef. This characterization station is composed of two primary components: the preamplifier box that measures the charge collected by a bias voltage across the sample and the DAQ box that samples the signals from the preamplifier box before passing them to a computer for analysis [11]. I determined that the characterization station has a gain of $534e^-/\text{mV}$, and a noise and pedestal value of $-1.99 \pm 0.60e^-$.

I characterized two diamond samples: CD-68 which was not irradiated and CD-17 which was irradiated with a fluence of 2.74×10^{15} 800 MeV p/cm^2. I performed these characterizations by placing a series of bias voltages across the samples to collect electron-hole pairs produced when β particles from a Sr-90 source passed through the diamond. As summarized in Table 5.1, the non-irradiated CD-17 sample had a total charge collected of $1920 \pm 18e^-$ when pumped for twenty-five hours. After irradiation, I measured the charge collected to be $1160 \pm 19e^-$, 60.4 % of the non-irradiated value. As illustrated in Figure 2.4, when silicon is irradiated with a similar fluence it has a smaller relative amount of charge collection compared to diamond. Without irradiation silicon has a maximum amount of collected charge of approximately $12300e^-$. After being irradiated with a total fluence of 1.3×10^{15}p/cm^2, this value for silicon decreases to approximately $5200e^-$, 42 % of the non-irradiated value. From these data, it becomes clear that diamond has a higher relative amount of collected charge after being irradiated with more than twice the fluence. This measurement of the diamond sample's higher charge collection indicates that diamond has utility as a potential upgrade to the vertex detectors in ATLAS.

In the course of this analysis, three characteristics of the diamond samples appeared that require a deeper look. These characteristics are the hysteresis presented in Figure 5.6, the effects of different pumping times on CD-17 in Table 5.1 and the different charge collections between the two samples illustrated in Figure 5.4. The hysteresis present in Figure 5.6 is the result of the capacitance and high resistivity

of the diamond sample [10]. While this hysteresis behavior provides different values for the charge collected depending on whether the voltage is increasing or decreasing, when diamond is used as a detecting medium, it is customary to use a bias voltage of $1V/\mu m$, which is the largest voltage used in the characterization. By not surpassing this $1V/\mu m$ limit, the hysteresis is removed. If the limit is surpassed, there is a risk that the sample will break down.

As Figure 5.4 illustrates, the two diamond samples CD-68 and CD-17 follow different charge collection curves when characterized. At a bias voltage of $1V/\mu m$, the non-irradiated CD-68 has a collected charge of $3870 \pm 32e^-$, while the non-irradiated CD-17 has a value of $1920 \pm 18e^-$. This difference between the amount of collected charge between two samples is likely the result of differences in the structures of the two diamonds as resulted of the CVD process.

Because exposure to radiation changes the structure of diamond, highly irradiated diamonds require greater pumping times to fully saturate deep traps [19]. This behavior is clearly illustrated in Figure 5.5. As summarized in Table 5.1, the pumping time for the irradiated CD-17 had an affect on the charge collection, varying from $950 \pm 16e^-$ for eighteen hours of pumping to $1160 \pm 19e^-$ for seventy-two hours of pumping. This relationship between the pumping time and collected charge indicates that a further research is necessary to determine the cutoff point at which the deep traps are saturated and further pumping is unnecessary.

In addition to being a replacement for vertex detectors in ATLAS, there is a general interest in using diamonds for various electronic components. In particular, there is an interest in using diamond for the dissipation of heat, where there is a requirement for a robust material to conduct heat from a source to a sink [8]. Diamond is also been used as a material for beam condition monitors [20] and luminosity monitors [21] in particle accelerators.

Bibliography

[1] M. L. Mangano, "The super-LHC", Contemporary Physics, 51:3, 211-231 (2010).

[2] `http://public.web.cern.ch/public/en/LHC/LHC-en.html` 4/12/2012.

[3] ATLAS Collaboration, "The ATLAS Experiment at the CERN Large Hadron Collider", JINST 3 S08003 (2008).

[4] `http://atlas.web.cern.ch/Atlas/GROUPS/UPGRADES/` 4/12/2012.

[5] H. Hoedlmoser et al. "Characterization of 150 μm thick epitaxial silicon pad detectors from different producers after 24 GeV/c proton irradiation" 10th RD50 Workshop, Vilnius, Lithuania, 4-6 June 2007.

[6] The RD-50 Collaboration, "Radiation hard semiconductor devices for very high luminosity colliders", CERN-LHCC-2010-012 ; LHCC-SR-003. - 2010. - 73 p.

[7] M. Barbero et al. *(The RD-42 Collaboration)*, "Development of Diamond Tracking Detectors for High Luminosity Experiments at the LHC", LHCC-RD-016; CERN-LHCC-2008-005. (2008).

[8] R. J. Tapper, "Diamond detectors in particle physics", Rep. Prog. Phys. **63**, 1273-1316 (2000).

[9] M. Werner and R. Locher, "Growth and application of doped and undoped diamond films", Rep. Prog. Phys. **61** 1665710.

[10] D. Meier et al., "Proton Irradiation of CVD Diamond Detectors for High Luminosity Experiments at the LHC", CERN/EP 98-79 (1998).

[11] `http://www.nikhef.nl/~i56/` 4/12/2012. **Note:** The manual and associated files may be found as a .zip file under **Documentation**: "Design plans of Nikhef characterisation station"

[12] C. T. Kelley, *Iterative Methods for Optimization*, SIAM Frontiers in Applied Mathematics, no 18, 1999.

[13] G. Arfken and H. Weber, *Mathematical Methods for Physicists*, Academic Press, 6 edition, 2005.

[14] L. Landau, "On the energy loss of fast particles by ionization". J. Phys. (USSR) **8**, 201 (1944).

[15] S. Meroli, D. Passeri, and L. Servoli, "Energy loss measurement for charged particles in very thin silicon layers", Journal of Measurements, **6** (1-3) (2011).

[16] John R. Taylor, *An Introduction to Error Analysis*, University Science Books, 1997.

[17] D. Hanselman, B. Littlefield, *Mastering MATLAB 7*, Pearson Prentice Hall, 2005.

[18] M. Marinelli et al., "Systematic study of the normal and pumped state of high efficiency diamond particle detectors grown by chemical vapor deposition", J. Appl. Phys., **89** 2, 1430-1435 (2001).

[19] M. Friedl, *Diamond Detectors for Ionizing Radiation*, University of Technology, Vienna, Austria (1999).

[20] A. Gorisek, et al., "ATLAS Beam Condition Monitor," Nucl. Instr. and Meth. A 572 (2007) 67-69.

[21] E. Bartz et al., "The PLT: A Luminosity Monitor for CMS Based on Single-Crystal Diamond Pixel Sensors," Nucl. Phys. B Proc. Suppl 197 (2009) 171-174.